

# On the Roles of Oxidation and Vaporization in Surface Micro-structural Instability during Solution Heat Treatment of Ni-base Superalloys

NEIL D'SOUZA, DEAN WELTON, GEOFF D. WEST, IAN M. EDMONDS,  
and HANG WANG

Micro-structural instability at the surface that develops during solution heat treatment of a typical third generation Ni-base superalloy, CMSX10N has been reported. It is shown that elemental Ni vaporizes from the surface during solutioning leading to de-stabilization of  $\gamma$  phase. With increasing extent of vaporization, a phase mixture of  $\beta$ ,  $\gamma'$ , and the refractory (W and Re-rich) precipitates occur within the surface layers resulting in the complete breakdown of the cuboidal  $\gamma/\gamma'$  phase morphology that is usually observed. It is demonstrated that the conditions at the surface have a marked effect on the vaporization kinetics and subsequent evolution of surface phases—the presence of a continuous dense oxide such as  $\text{Al}_2\text{O}_3$  or the presence of sacrificial Ni-foils interspersed in the furnace significantly suppresses elemental vaporization from the sample surface.

DOI: 10.1007/s11661-014-2554-0

© The Minerals, Metals & Materials Society and ASM International 2014

## I. INTRODUCTION

THE newer generations of Ni-base single-crystal superalloys, such as CMSX10N, were designed specifically for improved creep strength and therefore contain increasing amounts of refractory alloying elements such as Re, Ta, and W.<sup>[1]</sup> However, the significant partitioning behavior of elements, such as Ta and notably Re, results in a severely segregated as-cast microstructure and non-equilibrium inter-dendritic eutectic phases.<sup>[2–6]</sup> Therefore, a homogenization treatment is required to dissolve the eutectic and to eliminate the cored microstructure. During solutioning, the alloy is heated to the  $\gamma$  phase field above the solvus temperature. The dissolution of the non-equilibrium phases occurs along with homogenization of the microstructure and is governed by long-range diffusion of solute. Following solutioning, subsequent aging treatments are carried out on the homogenized alloy to precipitate  $\gamma'$  from the  $\gamma$  matrix at lower temperatures, where the main aim is to obtain the optimum cuboidal  $\gamma/\gamma'$  morphology required for high-temperature creep strength.

While there are extensive studies that consider the kinetics of homogenization and dissolution of eutectic phases within the bulk microstructure,<sup>[7–10]</sup> it has been

recently shown that a very different response is exhibited by the surface, where an anomalous microstructure develops following solutioning.<sup>[11]</sup> Specifically, de-stabilization of  $\gamma$  phase was observed, and the surface layer showed a mixture of  $\gamma'$  and refractory-rich precipitates, which is markedly absent within the bulk of the sample. The stabilization of  $\gamma'$  arises from enrichment in Al, while the formation of refractory-rich TCP phases incorporates the excess W and Re. To account for the evolution of this microstructure, it was proposed therefore that volatilisation of Ni and Cr occurs from the surface during solutioning, which is consistent with the high vapor pressures for both these elements in vacuum.<sup>[12]</sup> It is common practice therefore for solution heat treatment to be carried out under a partial pressure of an inert gas, such as Ar rather than in vacuum to prevent the volatilisation of high vapor pressure elements, such as Cr from the surface of a casting. A particular application where this principle is critical is in brazing, where the elemental vapor pressure is quite high at the melting point of these alloys.<sup>[13, 14]</sup> Other applications, where elemental vaporization is also critical is in electron beam melting; *e.g.*, in refining of Ti-base alloys, where evaporation of Ti from the liquid residing in the hearth occurs, in a vacuum atmosphere.<sup>[15]</sup>

This clearly demonstrates that “surface effects” need to be considered, and the notion of a “closed system” for mass balance considerations might not necessarily be correct. However, notwithstanding this preliminary study,<sup>[11]</sup> many aspects remain un-answered. The principal ones being;

- Solutioning is not carried out strictly in vacuum, but there is the localised circulation of Ar (carrier gas) and therefore, vaporization kinetics cannot be determined

---

NEIL D'SOUZA, Materials Technologist, DEAN WELTON, Turbines Metallurgist, and IAN M. EDMONDS, Engineering Manager Materials (Nuclear), are with the Rolls-Royce plc, PO Box 31, Derby, DE24 8BJ, U.K. GEOFF D. WEST, Research Fellow, is with the Loughborough University, Loughborough, Leicestershire LE11 3TU, U.K. HANG WANG, is with the School of Metallurgy and Materials, University of Birmingham, Birmingham B15 2TT, U.K. Contact e-mails: wanghang84@hotmail.com, h.wang.5@bham.ac.uk  
Manuscript submitted March 3, 2014.

Article published online September 13, 2014

in a straightforward manner using the Langmuir equation.<sup>[16]</sup>

- The nature and type of the as-cast oxide will have a profound effect on the rate of vaporization; the casting surface is covered in part by an Al<sub>2</sub>O<sub>3</sub> reaction layer, while in some regions, where mold/metal separation had occurred during casting, a “scaled” NiO layer is observed which arises from subsequent oxidation of the bare surface.<sup>[17]</sup>
- The as-cast microstructure at the surface of the casting varies; in some cases a layer of eutectic is observed “proud” of the secondary dendrite arms, unlike in other instances, the microstructure comprises dendrites and intermittent inter-dendritic channels (eutectic phases) that abut the surface.<sup>[18]</sup>

The purpose of this article is to elucidate these aspects more clearly. Specifically;

- (i) The occurrence of vaporization is demonstrated unambiguously through a novel experiment where the Ni vapor pressure in the furnace chamber can be varied to study the effect on vaporization.
- (ii) The role of the surface oxide in vaporization is also demonstrated through carefully controlled pre-oxidation experiments and possible mechanisms assessed.
- (iii) Finally, the resultant solute re-distribution within the surface layers that follow vaporization is quantitatively dealt with using a simplified approach to determine the evolution of phases, and limitations of this method are outlined.

In this study, the third generation alloy, CMSX10N whose nominal composition is given in Table I is considered owing to its prevalence as the alloy of preference for intermediate pressure turbine blades, where this effect is often observed. It is also worth highlighting that there are consequences arising from such an anomalous morphology on the surface of turbine blades developing during heat treatment. The decreased aerofoil section thickness with the optimum cuboidal  $\gamma/\gamma'$  morphology results in a reduction in thickness of the load-bearing cross-section of the aerofoil during service and subsequently having a detrimental effect on creep properties.

## II. EXPERIMENTAL

### A. Casting and Heat Treatment Experiments

Directional solidification was carried out at the Precision Casting Facility, Rolls-Royce, plc, Derby, UK. Cylindrical test bars (70 mm in length with a 10 mm diameter) were cast in an industrial directional solidification furnace. The basic parameters included the

following; furnace heater temperature nominally 1773 K (1500 °C), vacuum level of the furnace chamber was maintained at 0.1 Pa ( $10^{-6}$  atm), and a mold withdrawal rate of around  $5 \times 10^{-5}$  m s<sup>-1</sup> was used. Additional details are available elsewhere.<sup>[14]</sup> Solution heat treatment of the samples was carried out in a TAV vacuum furnace at the University of Birmingham, UK. All solutioning experiments were conducted in an Ar atmosphere at a pressure of  $2 \times 10^{-4}$  atm (0.2 mBar). The test bars were located in alumina boats and positioned in the center of the furnace, which was fitted with eight thermocouples at the corners and one at the center of the load. The heat treatment cycle consisted of a ramp with intermediate temperature holds followed by an isothermal hold at the final solutioning temperature, 1633 K (1360 °C). The time corresponding to the ramp cycle was 10 hour and this was subsequently followed by a 1-hour hold at 1633 K (1360 °C). Quenching at the end of the soak cycle was done using a forced argon flow resulting in a cooling rate of approximately 90 K min<sup>-1</sup>. In a second experiment, the test bars were positioned in alumina boats as before; however, dispersed sheets of Ni-foils were interspersed between the test bars. The thickness of the foil was 100  $\mu$ m. In yet another experiment, the test bars were pre-oxidised prior to solutioning and subsequent solutioning carried out in the absence of Ni-foil. This was done both in air as well as in a partial pressure of Ar. In the case of air, a standard Carbolite muffle furnace at the Precision Casting Facility (Derby), Rolls-Royce plc, Derby, UK was used. The samples were heated at 10 K min<sup>-1</sup> upto 1373 K (1100 °C) followed by an isothermal hold for 4 hour, after which the samples were air-cooled to ambient temperature. In the latter, this was done in a standard Vacuum Furnace Engineering vacuum furnace at Turbine Surface Technologies Limited, Nottingham, UK. The samples were heated at 10 K min<sup>-1</sup> under an Ar atmosphere at a partial pressure of  $5 \times 10^{-4}$  atm (0.5 mBar). The samples were held to 1373 K (1100 °C) for 4 hour and subsequently vacuum cooled to ambient temperature.

### B. Micro-structural Characterization

#### 1. Orientation measurement (Electron Back-Scatter Diffraction)

Aerofoil cross-sections for micro-structural characterization were prepared by initial grinding using SiC paper and a final polishing using 9 and 3  $\mu$ m diamond paste. For electron back-scatter diffraction (EBSD), the samples were mechano-chemically polished using colloidal silica on a Vibromet for 8 hours. All scanning electron microscopy (SEM) analyses were performed using a dual beam (FEI Nova 600 nanolab) scanning electron microscope. Back-scatter electron images (BEI) were collected using a retractable solid-state

Table I. Nominal Composition (Weight Percent) of Alloying Elements in CMSX10N

Alloy	Al	Co	Cr	Ti	Mo	Ta	W	Re	Ni
CMSX10N	5.9	3.1	1.6	0.1	0.45	8.5	5.5	6.8	bal

back-scatter detector using high (20 kV) and low (5 kV) electron beam accelerating voltages; the images collected at lower voltages possessed increased grain channeling contrast, while those at the higher voltage possessed increased compositional contrast. Chemical analysis was undertaken in this system at 20 kV using a 50 mm<sup>2</sup> Octane Silicon Drift Detector (SDD) from EDAX. Kikuchi patterns for EBSD were collected using a Hikari XP camera (EDAX). Patterns were collected and indexed according to the Ni structure file at a rate of 300 frames sec<sup>-1</sup>. A beam voltage of 20 kV with a current of 6.6 nA was used. The working distance varied between 5 and 10 mm. Orientation data were collected and analysed using OIM software (version 6.2) from EDAX. Images were displayed without cleaning as image quality (IQ) and image quality overlaid with grain orientation (inverse pole figure) maps.

## 2. Transmission Electron Microscopy (TEM)

To study the grain boundary chemistry in the thermally grown oxide (TGO), transmission electron microscopy (TEM) was used. A sample was prepared perpendicular to the TGO layer using a FEI Nova 600 Nanolab dual beam focussed ion beam (FIB) field emission gun scanning electron microscope equipped with an omniprobe micromanipulator. A standard in situ lift out procedure was used to extract the lamellar, attach it to a copper omniprobe half grid and thin to electron transparency. Care was taken to ensure that the sample prepared had a uniform thickness of around 200 nm. In addition TEM samples of the oxide layer on un-mounted samples from scaled and un-scaled regions were prepared in a similar way.

TEM analysis was conducted in a FEI Tecnai F20 operating at 200 kV. The system was operated in STEM mode, and complementary bright field (BF) and high angular annular dark field (HAADF) images were collected. Chemical analysis was undertaken in the system using a windowless Xmax 80N energy dispersive spectroscopy (EDS) SDD. To assess the chemical variation across the sample, spectrum maps of the sample and line-scans across grain boundaries were collected under high current conditions without pulse pile up correction. In addition to maximum sensitivity, the composition of a grain boundary was compared to that of the grain interior by collecting for 30 seconds live time.

## III. RESULTS

### A. Microstructure Evolution within the Surface Layer

The macrostructure corresponding to test bars in the open boat is shown in the BEI in Figure 1(a)—its surface has an “undulating” morphology (inset). Three distinct layers are observed as one transverses from the surface to the matrix; top layer (white box), intermediate layer (white dotted box) and a polycrystalline layer (white circle) growing into the substrate. The polycrystallinity observed in the BEI mode arises from imaging with a low energy incident electron beam (5 kV),

resulting in enhanced channelling contrast. The following points can be made:

- (i) The surface layer is clearly polycrystalline in nature and grows into the substrate, as is evident from EBSD derived inverse pole figure (IPF) map in Figure 1(d).
- (ii) The morphology nearest the un-transformed substrate (representative of white circle) is upto 200  $\mu\text{m}$  in thickness, and consists of  $\gamma'$  phase and blocky refractory-rich (W and Re) phases. This is seen in the lower portion of Figure 1(c).
- (iii) The layer above this morphology is referred to as the intermediate layer (representative of dotted white box) and is  $\sim 50 \mu\text{m}$  thick and corresponds to the upper portion of Figure 1(c). It consists of three phases: (a) the bright particles are refractory-rich (W and Re) TCP phases having a speckled morphology, (b) the gray lamellar structure is  $\gamma'$  phase ( $\frac{[\text{Ni}]}{[\text{Al}]} = \frac{67}{15}$  atomic ratio from EDS analysis), and (c) the dark matrix is  $\beta$ ; as determined from the  $\frac{[\text{Ni}]}{[\text{Al}]} = \frac{58}{36}$  atomic ratio from EDS analysis.
- (iv) The topmost layer (representative of solid white box) above the intermediate layer has a thickness  $\sim 50 \mu\text{m}$  and corresponds to the  $\beta$  phase as determined from the  $\frac{[\text{Ni}]}{[\text{Al}]} = \frac{58}{36}$  atomic ratio from EDS analysis. Dispersed  $\text{Al}_2\text{O}_3$  stringers having the black inter-woven morphology also exist at the periphery of the  $\beta$  grains, Figure 1(b). Importantly, at the interface between the top and intermediate layer, extensive porosity and cracks are observed (Figure 1(a)).

An important inference therefore follows from (ii), (iii), and (iv)—the original surface of the test bar is defined by the extremity of the intermediate layer, *i.e.*, the boundary between the intermediate layer and the topmost layer demarcates the surface of the test bar (cracked interface). It follows therefore that the top layer ( $\beta$  phase) constitutes a condensate that forms on the surface of the test bar. The polycrystalline nature of the  $\beta$ -grains within the top layer arises since  $\beta$  phase condenses from the vapor phase in the form of crystals with a large range in orientations during quenching. Subsequent oxidation of these polycrystalline  $\beta$  grains occurs in situ during cooling following quenching to form  $\text{Al}_2\text{O}_3$  (dispersed  $\text{Al}_2\text{O}_3$  stringers), which is unequivocal evidence for the formation of the condensate layer (Figure 1(b)).

The condensate layer gives valuable insight into the elemental species that have vaporized. Figure 2(a) refers to a plan view of the surface of the bar and clearly shows the “cauliflower-type” morphology of the condensate  $\beta$  layer. A similar morphology was also observed on the surface of a ceramic tile in the line-of-sight of the test bar that also served to trap the condensate (cold trap) during the quench. A cross-section through this layer is presented in Figure 2(b). Here, the outer Pt layer is deposited during FIB milling of the trench, and the  $\text{Al}_2\text{O}_3$  substrate (tile) is annotated in Figure 2(b). Transmission electron microscopy (TEM) foils were prepared

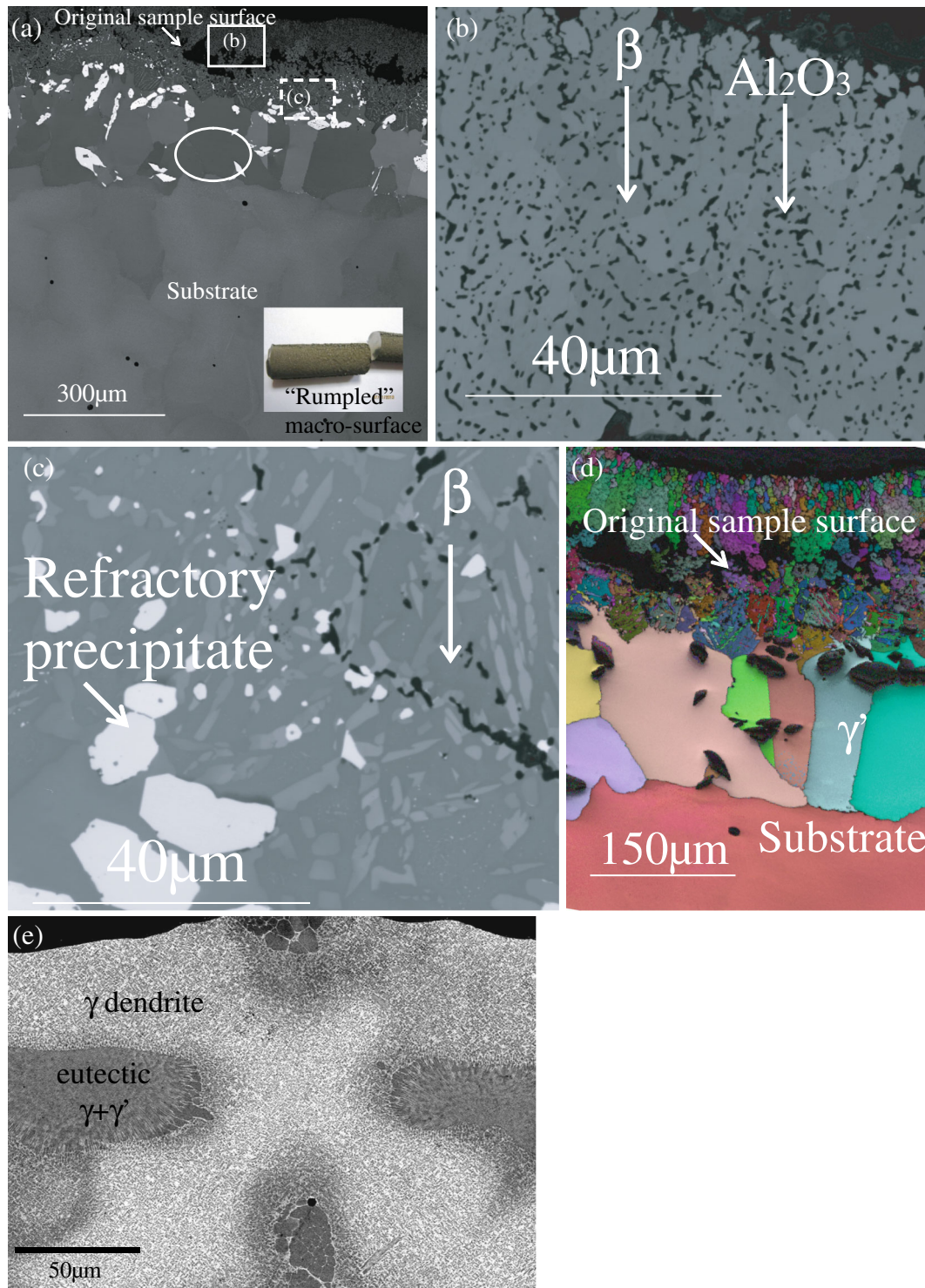


Fig. 1—BEI and an EBSD map of a cross-section of the sample placed in an open alumina boat and solution heat treated and BEI of a cross-section corresponding to the as-cast condition. (a) BEI of the surface defect showing an undulating surface morphology; (b) BEI showing the top layer comprising  $\beta$  phase with dispersed  $\text{Al}_2\text{O}_3$  stringers (solid white box); (c) BEI showing the intermediate layer having bright refractory-rich phases, light gray  $\gamma'$  and the dark  $\beta$  matrix (dotted white box), and polycrystalline layer  $\beta$  comprising  $\gamma'$  phase and blocky refractory-rich precipitates (white circle); (d) EBSD derived IQ/IPF composite map showing the various orientations at the surface compared to the substrate (red box); (e) BEI of the as-cast test bar showing  $\gamma$  dendrite and inter-dendritic eutectic ( $\gamma + \gamma'$ ) region.

from this region and the composition determined using EDS. Ten positions were chosen within the foil and the compositions (at. pct) are as follows; Al = 38.4,

Cr = 0.9, Co = 1.9, and Ni = 58.7. While there is vaporization of Cr and Co, this loss is minor when compared to that of Ni and Al and from the EDS

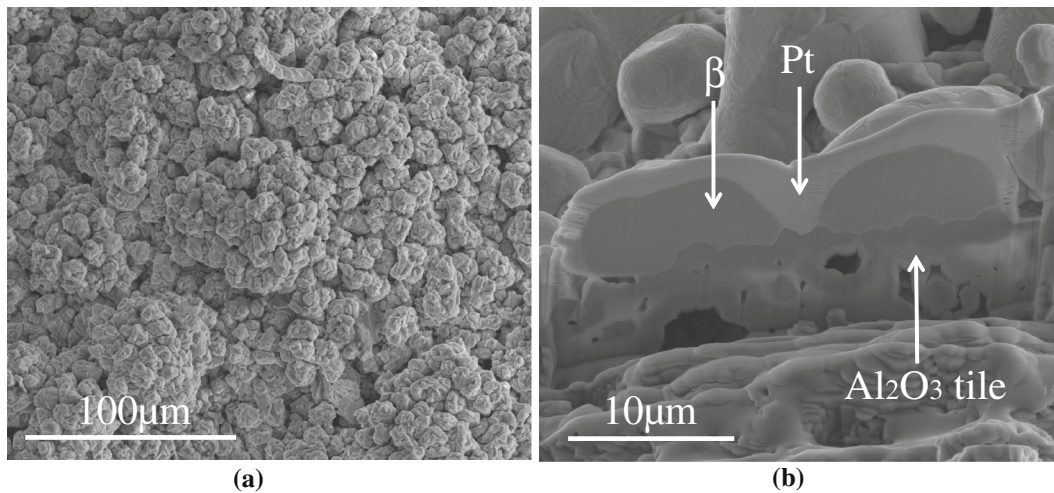


Fig. 2—SEM and FIB-SEM analysis of  $\beta$  condensate. (a) Plan view micrograph of the surface of the sample showing the “cauliflower type” morphology of  $\beta$  condensate; (b) SEM micrograph of a FIB prepared cross-section through the ceramic tile used as a cold trap for the  $\beta$  condensate. This FIB cross section was subsequently lifted out for analysis in the TEM.

determined atomic ratios, it is seen once again that this condensate layer was  $\beta$  phase, *i.e.*,  $\left[\frac{\text{Ni}}{\text{Al}}\right] = \left[\frac{38}{38}\right]$ , cf. measurements on cross-section of the bar.

Since the condensate layer is  $\beta$  phase, there must be vaporization of both Ni and Al from the surface of the bar during solutioning. The extent of vaporization is determined by the vapor pressure, and in vacuum, it is given by the Langmuir equation.<sup>[16]</sup> In case of ideal solid solutions, this can be modified to consider the respective mole-fractions. However, in the case of non-ideal solutions, this is not straightforward, since interactions between the solute elements have to be considered, and reliable experimental data are lacking. Also importantly, the nature *i.e.*, porosity and volatility of the native surface oxide will also have a marked effect on the vaporization rate from the surface of the bar. Both these aspects have to be considered.

Also for comparison, a low magnification BEI corresponding to the cross-section of a test bar in the as-cast condition is given in Figure 1(e). It clearly shows the dendrite cross-section, which is segregated in W and Re (bright contrast), and there is the presence of the interdendritic eutectic ( $\gamma + \gamma'$ ) between the dendrite lobes both within the bulk cross-section as well as isolated channels between abutting dendrite lobes at the surface. This again reinforces the fact that micro-structural instability exclusively develops at the surface during solutioning.

### B. Characterization of Surface Oxides

The extent of vaporization is dictated by the nature of the oxide on the surface of the bar, since some oxides present a physical barrier to elemental loss. The test bars in these solutioning experiments were directionally solidified in single crystal form. Under these processing conditions, it has been shown that different oxides characterize the surface, *i.e.*, the so-called “scaled” and “un-scaled” regions. The formation of the type of oxide is governed by mold/metal separation that occurs during

mold withdrawal from the furnace during casting.<sup>[17]</sup> When the mold and metal are in contact, a reaction layer of  $\text{Al}_2\text{O}_3$  forms on the surface of the casting (formed by the reaction between  $\text{SiO}_2$ -based mold prime coat and Al in the metal) and referred to as un-scaled region, but in regions where the metal has subsequently delaminated from the mold wall, this layer is stripped from the metal surface and retained on the mold wall. The “bare” surface of the casting subsequently undergoes rapid transient oxidation resulting in the formation of an outer NiO and an inner mixed Ni, Cr, Ta, Al-based spinels, and referred to as the scaled region, owing to its texture.<sup>[17]</sup> Such oxides exist over the surface of the test bars prior to solutioning, and it is therefore, important to ascertain the thickness and the extent of coverage of these oxides across the surface in more detail.

Figure 3(a) is a HAADF STEM micrograph of a sample prepared from the scaled region and clearly shows the dual oxide layer. The outer oxide is NiO, and the EDS spectrum acquired from this region also shows some solubility of Co; Figure 3(b). The Cu peak is an artifact and arises from X-rays generated from the Cu-grid used for the TEM samples. On the other hand, the inner oxide shows a highly convoluted and inter-woven morphology. A characteristic EDS spectrum from this region shows that this oxide comprises Ni, Al, and Cr; Figure 3(c). This fine morphology coupled with similar lattice parameters of the spinel phases preclude analyses by diffraction using selective area diffraction mode in the TEM to uniquely identify these mixed oxides; however, mixed oxides of  $\text{CrTaO}_4$ ,  $\text{NiAl}_2\text{O}_4$ , and  $\text{AlTaO}_4$  have been reported by Younes *et al.*<sup>[19]</sup> during oxidation of the third-generation alloy, CMSX10K upto 50 hours. The un-scaled region on the other hand presents a more interesting proposition. The existence of the  $\text{Al}_2\text{O}_3$  reaction layer, which is adherent to the surface should present a “physical” barrier to elemental vaporization, if it occurs uniformly across the surface. Two aspects were therefore considered;

(a) To determine the extent of coverage of the  $\text{Al}_2\text{O}_3$  reaction layer on the un-scaled region of the as-cast surface, the bar was in the un-blasted condition, and in this instance, pre-oxidation was done in air. The rationale being that within the un-scaled regions where the  $\text{Al}_2\text{O}_3$  reaction layer had locally spalled off from lack of adherence, following removal of the test bar from the mold, subsequent oxidation in air would result in the formation of a duplex oxide layer, with an outer layer of NiO in these regions. Figure 4(a) is a micrograph that is a plan view of the surface and clearly shows different oxide morphologies. The dark regions refer to  $\text{Al}_2\text{O}_3$ , while the bright regions clearly appear “raised” and show a fine-grained structure. A slice perpendicular through the surface through this oxide using FIB (ion beam image) is presented in cross-section in Figure 4(b), and the spectra corresponding to the different

regions through the slice indicate an outer NiO (dissolved Co) and an inner mixed Ni, Al, Cr, and Ta oxide. Therefore, from Figure 4(a), it is clear that the reaction layer coverage is poor, and there is an appreciable portion within the un-scaled region, where the  $\text{Al}_2\text{O}_3$  reaction layer had indeed spalled. However, where  $\text{Al}_2\text{O}_3$  is observed in Figure 4(a), this corresponds to the reaction layer formed during casting that has adhered to the metal surface even during removal of the test bar from the mold. An important inference can therefore be made—the initial  $\text{Al}_2\text{O}_3$  reaction layer is not continuous; otherwise after pre-oxidation, the un-scaled region would have only comprised  $\text{Al}_2\text{O}_3$ . This is unexpected since during mechanical separation of the test bar from the mold following casting, intermittent delamination of the reaction layer from the surface of the bar is most likely to occur owing to its poor adherence to the metal substrate.

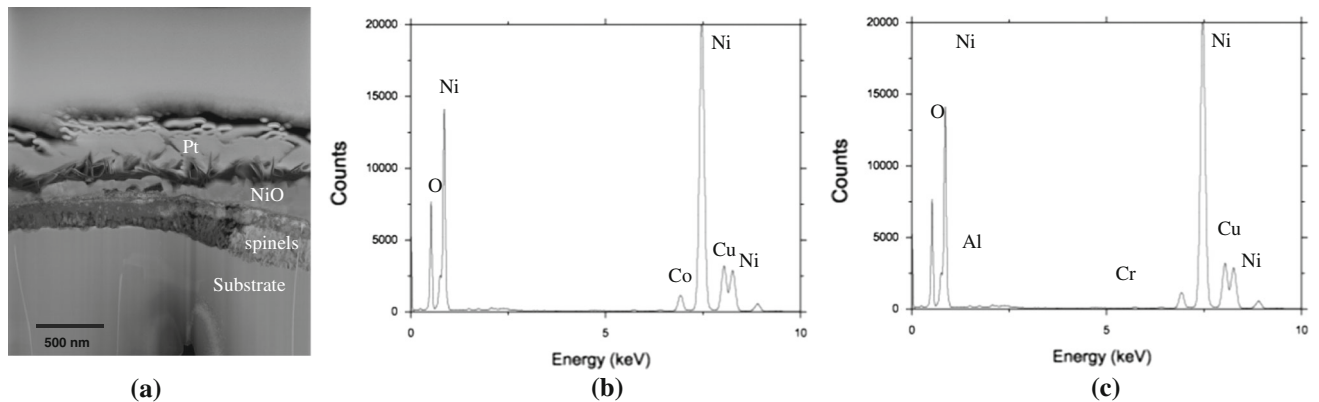


Fig. 3—TEM micrograph of the scaled region clearly showing the dual oxide layer. (a) HAADF STEM micrograph from the scaled region; (b) EDS spectrum from the outer oxide shows some solubility of Co; and (c) EDS spectrum from the inner oxide indicates that the oxide comprises of Ni, Al, Cr.

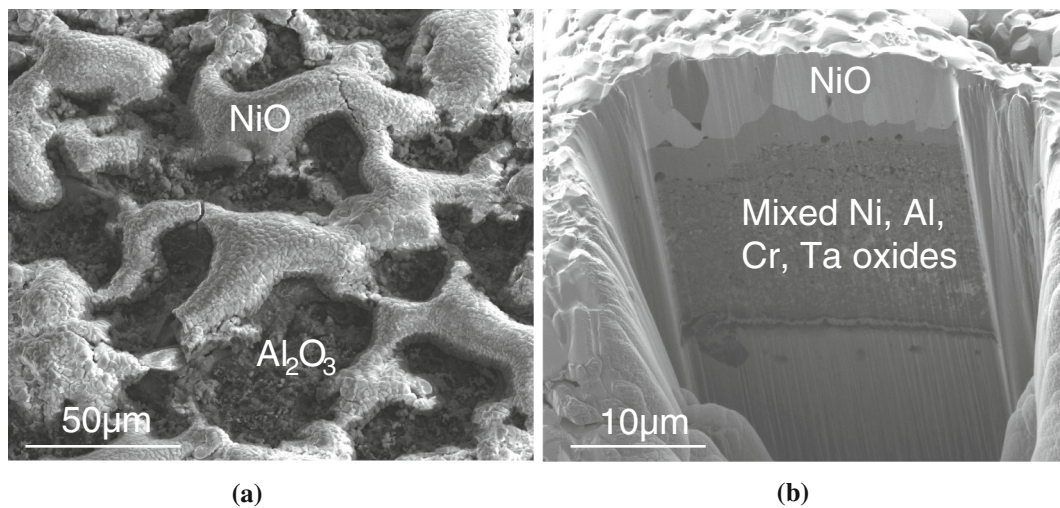
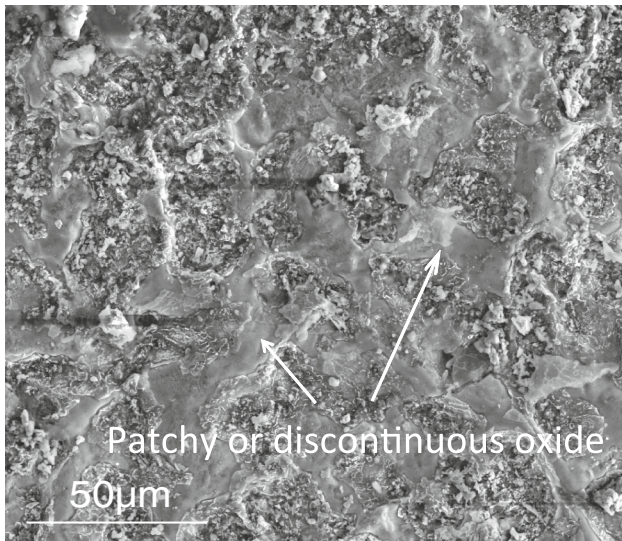
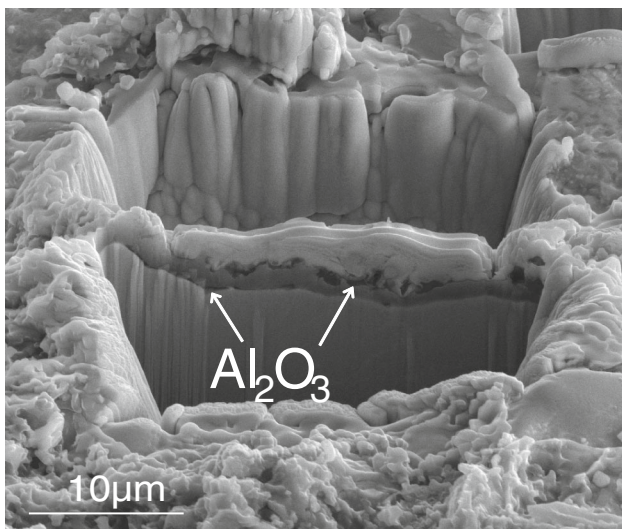


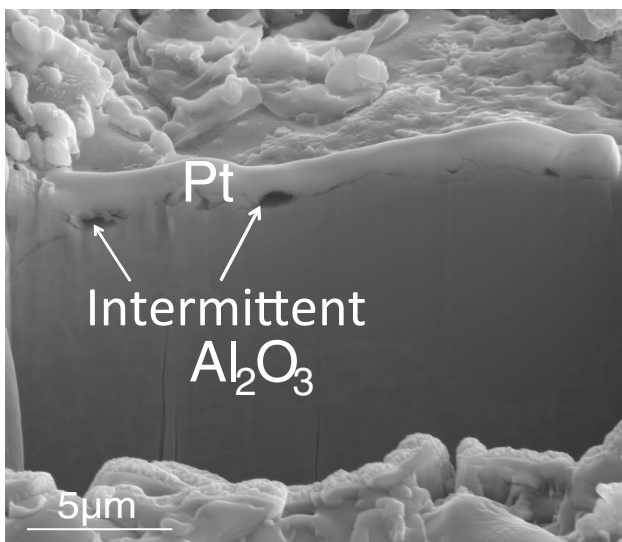
Fig. 4—SEM and FIB-SEM images of a sample pre-oxidised in air (a) Plan view micrograph of the surface of the pre-oxidised sample. EDS showed that the dark regions correspond to  $\text{Al}_2\text{O}_3$ , while the bright regions that sit “proud” of the  $\text{Al}_2\text{O}_3$  are NiO; (b) Ion beam induced secondary electron image of a FIB section cut through the NiO layer surface showing the evolution of a multi-layer oxide.



(a)



(b)



(c)

◀Fig. 5—SEM images of a sample pre-oxidised in an Ar atmosphere. (a) Plan view micrograph of the surface showing the presence of a discontinuous oxide layer; (b) and (c) show a FIB section sliced perpendicular to the surface highlighting the intermittent nature of the  $\text{Al}_2\text{O}_3$  layer.

blasting. Pre-oxidising using Ar before solutioning can be used to form an  $\text{Al}_2\text{O}_3$  layer across the surface and accordingly an as-cast test bar was pre-oxidised in Ar at a temperature of 1373 K (1100°C) for 4 hour. Under these conditions, the only thermodynamically stable oxide is  $\text{Al}_2\text{O}_3$ . The oxide growth kinetics is given by the parabolic rate constant,  $k_p$ . At 1373 K (1100 °C),  $k_p \sim 10^{-9} \text{ g}^2 \text{ cm}^{-4} \text{ s}^{-1}$  for NiO and  $k_p \sim 10^{-12} \text{ g}^2 \text{ cm}^{-4} \text{ s}^{-1}$  for  $\alpha\text{-Al}_2\text{O}_3$ .<sup>[20]</sup> Typically, at 1273 K (1000 °C), where  $\gamma$  and  $\theta\text{-Al}_2\text{O}_3$  are also stable,  $k_p \sim 5 \times 10^{-14} \text{ g}^2 \text{ cm}^{-4} \text{ s}^{-1}$  for  $\alpha\text{-Al}_2\text{O}_3$ , which is two-orders of magnitude lower than that for (transitional)  $\gamma$  and  $\theta\text{-Al}_2\text{O}_3$ .<sup>[21]</sup> It is clear that the growth kinetics of  $\alpha\text{-Al}_2\text{O}_3$  is the most stable polymorph in orders of magnitude smaller than that of NiO or CoO. Therefore, the coverage of  $\alpha\text{-Al}_2\text{O}_3$  across the surface is non-uniform, and regions termed as “bare metal” have actually discontinuous or patchy oxide regions, compared to a continuous layer in other regions. This accounts for the prominent back-scattered signal arising from the metal in Figure 5(a), which corresponds to a BEI from the surface. Slices cut perpendicular to the surface through the bright and gray regions in Figure 5(a) are shown in Figures 5(b) and (c) respectively. EDS spectra in Figure 3(b) show the occurrence of an  $\text{Al}_2\text{O}_3$  layer of 1- $\mu\text{m}$  thickness corresponding to the bright region; however, there is very intermittent oxide corresponding to Figure 5(c), indicating only isolated coverage and not continuous. The inference is—even pre-oxidation in Ar does not result in a continuous  $\text{Al}_2\text{O}_3$  layer in these conditions owing to the slow growth kinetics.

### C. Conditions Affecting Microstructure Evolution within the Surface Layer

Since vaporization of both Ni and Al is occurring from the surface of the sample, by manipulating the local conditions at the surface of the test bar, the vaporization rate can be altered. One such method is the use of sacrificial Ni-foil interspersed between test bars that would result in Ni loss occurring principally from the surface of the foil and thereby altering the Ni vaporization from the sample. Another method relies on the growth of a dense oxide such as  $\text{Al}_2\text{O}_3$  prior to solutioning, which presents a barrier to elemental loss from the surface.

### D. Ni-Foil

The surface microstructure observed in this case showed some clear differences compared with that presented in Figure 1. Neither surface undulation nor

(b) Pre-oxidation in Ar was done on both as-cast (unblasted) as well as using blasted specimens; in the latter case, the surface is devoid of any oxide after

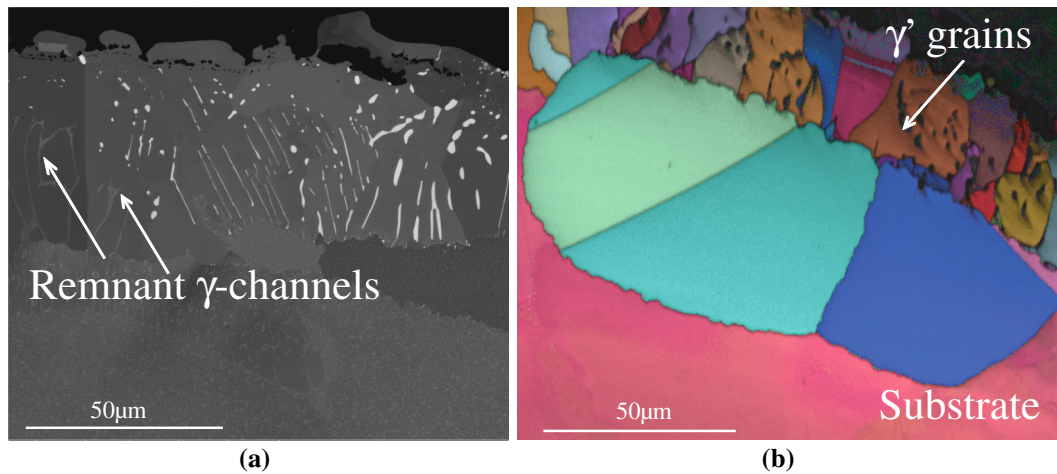


Fig. 6—BEI and an EBSD map of the cross section of sample in an open alumina boat dispersed with Ni-foil and heat treated. (a) BEI micrograph showing a surface layer comprising a  $\gamma'$  matrix and bright refractory-rich phases with the substrate seen beneath. Remnant  $\gamma$ -channels can be seen in the polycrystalline layer; (b) EBSD derived IQ/IPF map showing the differences in orientation compared to the surface.

a condensate layer was observed in this case. A typical cross-section is presented in the BEI in Figure 6(a), where unlike in Figure 1, only two layers are observed. The outermost layer comprises  $\gamma'$  and refractory-rich precipitates, and the morphology of these phases is less blocky. The condensate and the intermediate layer are notably absent, compared with Figure 1. Some evidence of re-crystallisation was also observed. The EBSD derived IPF map in Figure 6(b) shows that like in the previous instance the surface layer was polycrystalline; however, a marked reduction in the extent of micro-structural instability occurs at the surface. Two important points should be emphasised;

- (a) This is clear evidence of the role of vaporization in the evolution of the surface phases—by increasing the amount of Ni that can vaporize from the sacrificial foil, vaporization from the test bar surface was suppressed.
- (b) Morphological instability is only restricted to the surface, despite the presence of un-dissolved interdendritic phases within the bulk or the sporadic existence of eutectic phases across the surface of the bar. This categorically demonstrates that the development of micro-structural instability at the surface is *markedly independent* of alloy composition.

#### E. Pre-Oxidation

As mentioned in the preceding section, altering the nature of the surface oxide can have a pronounced effect on the extent of vaporization. Pre-oxidation in Ar to form  $\text{Al}_2\text{O}_3$  is another such method. Figure 7(a) is a BEI corresponding to such a condition, where there is the distinct absence of the outer condensate layer, and the occurrence of the intermediate layer [represented by white box in Figure 7(a)] is observed. In the later; Figure 7(b),  $\gamma'$  platelets occur within the  $\beta$ -phase matrix (intermediate layer) and followed by the polycrystalline

$\gamma'$  layer below growing into the substrate. Since the extent of coverage of  $\text{Al}_2\text{O}_3$  is non-uniform following pre-oxidation prior to solutioning for the given conditions (Figures 5(a), (b), (c)), this is expected to be less effective in suppressing elemental vaporization from the surface compared with the use of sacrificial Ni-foil during solutioning. Also, fragmentation of this intermediate layer during subsequent metallographic sample preparation is evident, *i.e.*, delamination of the intermediate layer from the polycrystalline  $\gamma'$  layer during quenching [cracked interface in (Figure 7(a))]. This is not surprising, given the differential volumetric contraction between  $\gamma'$  and  $\beta$  phases.<sup>[22]</sup>

It should also be pointed out that the as-cast surface is covered by two types of oxide, *i.e.*, a thermally grown duplex oxide (Figures 3(a) through (c)) corresponding to the scaled region and an  $\text{Al}_2\text{O}_3$  reaction layer referring to the un-scaled region.

- Reaction between the Al in the alloy and  $\text{SiO}_2$  prime coat of the mold wall (in contact with the metal) resulting in the formation of  $\text{Al}_2\text{O}_3$ , as detailed in Reference 17. This corresponds to the un-scaled region.
- On the other hand, when the metal separates from the mold wall in certain regions (where the  $\text{Al}_2\text{O}_3$  layer is now retained on the mold surface owing to lack of adherence with the metal), subsequent oxidation of the “bare” surface occurs resulting in the formation of a mixed oxide (transient oxidation of elements such as Ni, Co, Cr, and Al), resulting in loss of these elements from the surface.

However, there is no effect of de-alloying on the micro-structural instability that develops at the surface following subsequent heat treatment. Similar solutioning experiments were carried out on test bars with blasted surfaces, where the surface oxide, as well as upto 50  $\mu\text{m}$  of substrate beneath was mechanically abraded. A morphological instability identical to that presented in



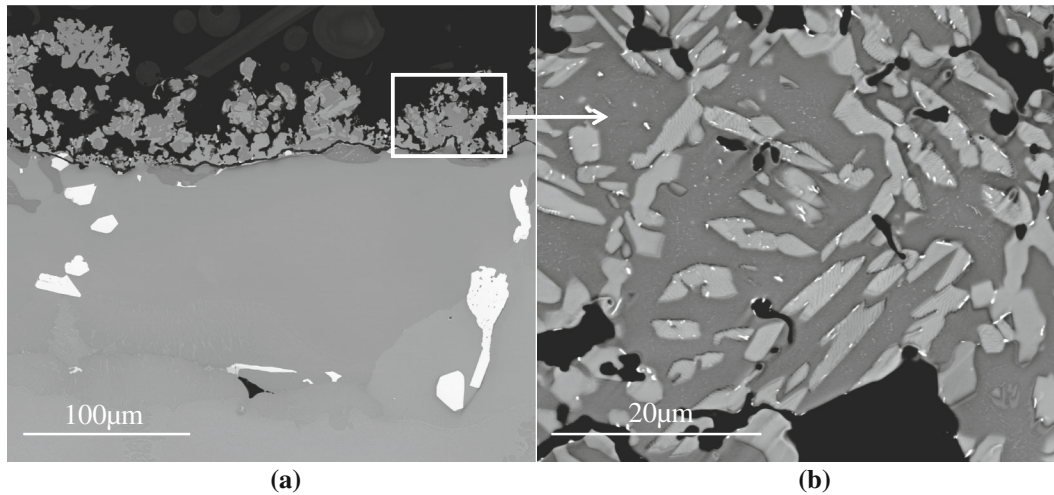


Fig. 7—BEI's of cross-section of the sample pre-oxidised in Ar and heat treated. (a) BEI of the surface morphology shows the absence of the outermost condensate layer (c.f. Fig. 1(a)) but with an intermediate layer; (b) BEI highlighting the presence of  $\gamma$  precipitates within the  $\beta$  matrix.

Figures 1(a) through (d) develops at the surface. The evolution of the surface morphologies was therefore independent of whether the surface was as-cast (un-blasted) or blasted.

#### IV. DISCUSSION

##### A. Role of Oxidation and Vaporization

The as-cast surface is characterized by two different types of oxide. A portion of the surface is covered by a duplex oxide—an outer NiO and internal mixed spinel-type and referred to the “scaled” region. The remainder of the casting surface comprises an  $\text{Al}_2\text{O}_3$  reaction layer and referred to as the “un-scaled” region. The latter arises as a reaction product from the reaction;  $4\text{Al}_{(L)} + 3\text{SiO}_2 = 2\text{Al}_2\text{O}_3 + 3\text{Si}_{(L)}$ , where the casting remains in contact with the mold wall. The subscript refers to the element dissolved in the liquid alloy, while  $\text{SiO}_2$  constitutes the binder in the ceramic shell system forming the mold cavity, which is in contact with the liquid metal. However, following solutioning, the only observed oxide is  $\text{Al}_2\text{O}_3$ , *i.e.*, there is the marked absence of the outer NiO.

The thermodynamic stability of NiO is dependent on the  $\text{O}_2$  partial pressure and de-stabilization of NiO can arise from either;

- (i)  $\text{NiO(s)} \rightarrow \text{Ni(s)} + \frac{1}{2} \text{O}_2(\text{g})$ , *i.e.*, dissociation
- (ii)  $\text{NiO(s)} \rightarrow \text{Ni(g)} + \frac{1}{2} \text{O}_2(\text{g})$ , *i.e.*, volatilisation

For the oxidation of Ni,<sup>[23]</sup>  $\text{Ni(s)} + \frac{1}{2} \text{O}_2(\text{g}) \rightarrow \text{NiO(s)}$   $\Delta G^0 = [-244, 550 + 98.5T]\text{J}$

$$\Delta G^0 = -RT \ln K = \frac{1}{2} RT \ln p_{\text{O}_2} \quad \text{or} \quad p_{\text{O}_2}(\text{Eqlb}) = e^{\frac{2\Delta G^0}{RT}} \quad [1a]$$

Therefore, for  $p_{\text{O}_2} < p_{\text{O}_2}(\text{Eqlb})$ , dissociation of NiO will occur.

Likewise, for volatilisation of NiO;

$$\Delta G^0 = -RT \ln K = -RT \ln [p_{\text{Ni}} \sqrt{p_{\text{O}_2}}]. \quad [1b]$$

Volatilisation of NiO can be considered from a combination of two reactions; dissociation of NiO and vaporization of Ni, *i.e.*,  $\text{Ni(s)} \rightarrow \text{Ni(g)}$ .

For Ni vaporization,<sup>[12]</sup>  $\text{Ni(s)} \rightarrow \text{Ni(g)}$   $\Delta G^0 = 2.303R[22, 606 - 10.576T + 0.38T \ln T]\text{J}$

$$\log p_{\text{Ni}}(\text{Eqlb}) = 15.701 - \frac{35,378}{T} - 0.8717 \log T - 0.5 \log p_{\text{O}_2} \quad \text{NiO vaporization} \quad [2]$$

$$\log p_{\text{Ni}}(\text{Eqlb}) = 10.557 - \frac{22,606}{T} - 0.8717 \log T \quad \text{Ni vaporization.} \quad [3]$$

Therefore, for  $p_{\text{Ni}} < p_{\text{Ni}}(\text{Eqlb})$ , vaporization of Ni or NiO or both will occur.

In Figure 8, the partial pressure of  $\text{O}_2$  and Ni corresponding to dissociation of NiO and vaporization of NiO and Ni are plotted with temperature (Eqs. [1a], [2] and [3]). In the case of vaporization of NiO (Eq. [2]), three different  $p_{\text{O}_2}$  values are considered, *i.e.*,  $10^{-5}$ ,  $10^{-7}$  atm and  $p_{\text{O}_2}$  corresponding to Eq. [1a]. The following points can be made;

- (a) With increasing temperature, the eqlb  $p_{\text{O}_2}$  above which NiO is stable (no dissociation) increases. Also, at a given temperature, for increasing eqlb  $p_{\text{O}_2}$  there is a decrease in eqlb  $p_{\text{Ni}}$ . Therefore, at the solutioning temperature to prevent dissociation of NiO,  $p_{\text{O}_2} > 4.4 \times 10^{-6}$  atm and to prevent vaporization of NiO,  $p_{\text{Ni}}(\text{max}) = 8.2 \times 10^{-7}$  atm
- (b) The total pressure in the furnace chamber ( $P$ ) =  $2 \times 10^{-4}$  atm. This is predominantly the pressure of Ar ( $P \sim p_{\text{Ar}}$ ); *i.e.*,  $p_{\text{O}_2}$  is at least an order of magnitude smaller

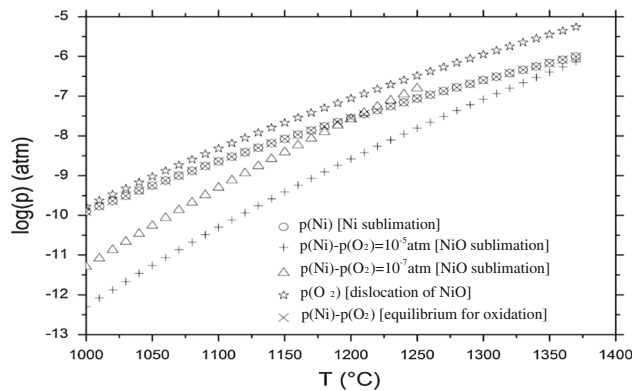


Fig. 8—Plot of critical partial pressure of oxygen to prevent dissociation of NiO with temperature and vapor pressure of Ni for sublimation of Ni and NiO corresponding to a range of oxygen partial pressures.

(i) At the solutioning temperature,  $p_{O_2} > 4.4 \times 10^{-6}$  atm to prevent dissociation of NiO. Therefore, for  $p_{O_2} > p_{O_2}$  (eqlb) to prevent dissociation of NiO;

- $p_{O_2} = 5 \times 10^{-6}$  atm,  $p_{Ni} = 7.7 \times 10^{-7}$  atm
- $p_{O_2} = 10^{-5}$  atm,  $p_{Ni} = 5.5 \times 10^{-7}$  atm

(ii) At an intermediate temperature, say 1523 K (1250 °C),  $p_{O_2} > 3.2 \times 10^{-7}$  atm to prevent dissociation of NiO. Therefore, for  $p_{O_2} > p_{O_2}$  (eqlb) to prevent dissociation of NiO

- $p_{O_2} = 5 \times 10^{-7}$  atm,  $p_{Ni} = 7 \times 10^{-8}$  atm
- $p_{O_2} = 10^{-6}$  atm,  $p_{Ni} = 5 \times 10^{-8}$  atm
- $p_{O_2} = 10^{-5}$  atm,  $p_{Ni} = 1.5 \times 10^{-8}$  atm

The eqlb  $p_{Ni}$  for volatilisation of NiO calculated for a range of  $p_{O_2}$  where NiO is stable is within an order of magnitude of the eqlb  $p_{Ni}$  for vaporization of Ni from the surface of the sample,  $8.7 \times 10^{-8}$  atm  $< p_{Ni} < 5.5 \times 10^{-7}$  atm in the temperature range; 1523 K (1250 °C)  $< T < 1633$  K (1360 °C) (Eq. [3]). It follows therefore that for the typical  $O_2$  partial pressures in the furnace chamber; either NiO will dissociate, or vaporization of NiO is most likely to occur and this phenomenon is more pronounced with increasing temperature. This is consistent with the experimental observations of the absence of NiO after solutioning.

The loss of NiO will subsequently facilitate vaporization of Ni, Co, and Cr from the surface of the bar. However, within the scaled region of the surface, there also exists an inner mixed spinel layer, which is also markedly absent from the surface of the bar. Oxidation studies in CMSX10 have reported the presence of mixed oxides such as, (Ni,Co)Ta<sub>2</sub>O<sub>6</sub>, (Ni,Co)WO<sub>4</sub>, CrTaO<sub>4</sub>, and Cr(Mo,W)O<sub>4</sub><sup>[24]</sup>; some of these elements have also been detected in the duplex oxide scale (Figure 3(c)), albeit it was not possible to uniquely identify these mixed oxides. The absence of these oxides suggests that

these have dissociated, but it is not possible to do detailed calculations owing to scarcity of reliable thermodynamic data, as well as not being able to uniquely identify the types of oxides. The un-scaled region on the other hand comprises Al<sub>2</sub>O<sub>3</sub>; therefore, the key aspect that needs to be addressed is vaporization in the presence of Al<sub>2</sub>O<sub>3</sub>. Two possibilities are critically examined;

(a) Vaporization through Al<sub>2</sub>O<sub>3</sub>—A number of crystallographic polymorphs of Al<sub>2</sub>O<sub>3</sub> exist depending predominantly on the oxidation temperature. The rhombohedral R3-c  $\alpha$ -Al<sub>2</sub>O<sub>3</sub> allotrope is the thermodynamically stable form stable form, which the other transitional phases will eventually convert to at given time and temperature.<sup>[25]</sup> It was not possible to determine the nature of Al<sub>2</sub>O<sub>3</sub>, owing to the thickness,  $< 1 \mu\text{m}$  in our experiments. One possibility therefore, is that in the case of  $\gamma$  or  $\theta$ -Al<sub>2</sub>O<sub>3</sub>, which grow at the oxide/gas interface (Al is transported to the surface), it might be possible for vaporization to occur, with elemental transport occurring via the Al<sub>2</sub>O<sub>3</sub> grain boundaries. Figure 9(a) is a BF STEM micrograph through the Al<sub>2</sub>O<sub>3</sub> layer showing the presence of three grains and two grain boundaries. A comparison of EDS spectra obtained from at a grain boundary and within a grain is presented in Figure 9(b). No significant differences are observed between the spectra collected in these two locations. Please note that the sum peaks in Figure 9(b) arise because of the addition of the O and Al signals owing to the very high number of counts. Small peaks corresponding to Ni and Cr are also observed in the spectra. These peaks are most likely to have been generated from stray electrons interacting with the “thick” Ni-base alloy which is located at the side of the electron transparent Al<sub>2</sub>O<sub>3</sub> region of interest. A similar process also leads to a Cu signal arising from the grid that the TEM sample is attached, as in Figure 3(b) and (c). This fact is further reinforced by the EDS line-scan that traverses the grains and grain boundary, where the number of counts for Al and O (Figure 9(c)) is at least two-orders of magnitude greater than for Ni, Co, and Cr (Figure 9(d)). It can be concluded therefore that the grain boundaries are not providing a short-circuit path for transport of the vaporizing species.

(b) Fracture of Al<sub>2</sub>O<sub>3</sub> during heating—Fracture of the oxide layer during heating to the solutioning temperature can result in mechanical de-bonding of the oxide from the surface and thereby facilitate vaporization. This mechanism was investigated by changing the ramp-rate. A twofold decrease in the heating rate upto the maximum solutioning temperature was adopted. However, no change in the surface morphology was observed. This is not unexpected since oxide spallation is driven by a significant biaxial compressive strain developed in-plane as a result of the coefficient of thermal expansion mismatch between substrate and oxide. This in turn leads to two locally discrete methods

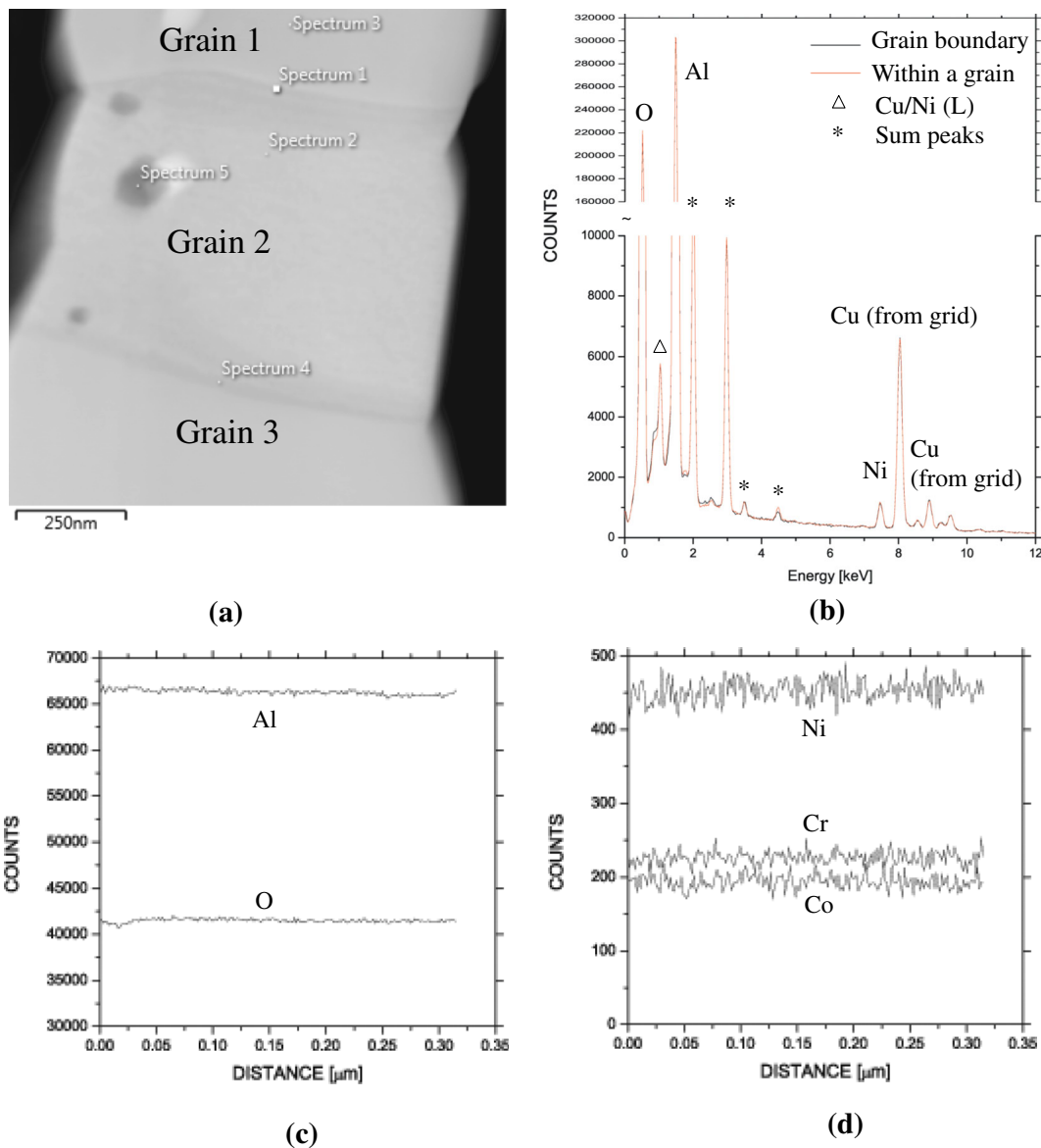


Fig. 9—(a) BF STEM micrograph through the  $\text{Al}_2\text{O}_3$  layer showing the presence of grains (and grain boundary), (b) Spectra from within the grain and at the grain boundary (please note there are 4 peaks labeled with \*, which are all pulse pile up peaks due to high count conditions to maximise sensitivity), (c) and (d) EDS line-scan corresponding to Al and O and Ni, Co, and Cr compositions, respectively, across the grain boundary.

for de-bonding, *i.e.*, buckling or wedging.<sup>[26]</sup> However, such a stress/strain state will only occur during cooling and not during heating.

It follows therefore from (i) and (ii) that elemental loss must necessarily occur from a surface that is devoid of  $\text{Al}_2\text{O}_3$ . In fact, this is borne out by our results—in the case of the scaled region, there is only the occurrence of the duplex oxide; *i.e.*, outer NiO and inner mixed Ni Al Cr Ta oxides. In the un-scaled region, notwithstanding the presence of  $\text{Al}_2\text{O}_3$ , there is clear evidence that this reaction layer is not continuous. This aspect is further confirmed by the Ar pre-oxidised experiment, where a similar situation occurs, *i.e.*, the coverage of  $\text{Al}_2\text{O}_3$  is not uniform. Elemental vaporization ceases, when a continuous  $\text{Al}_2\text{O}_3$  layer is formed, which is observed on the surface of the solution heat treated test bar.

## B. Sequence of Microstructure Evolution at the Surface

There is a marked variation in the phase evolution at the surface of the test bar; *i.e.*, intermediate layer, as in Figure 1, comprising a  $\beta$  matrix with  $\gamma'$  platelets and refractory-rich (W and Re) phases, while the layer beneath comprises  $\gamma'$  phase and blocky refractory-rich precipitates. After solutioning, there is micro-structural instability that develops at the surface. The sequence of evolution of the morphologies is presented in Figure 1(a). Neglecting the  $\beta$ -condensate layer that forms above the surface, within the surface layers there is the occurrence of the intermediate layer, as in Figure 1(a), comprising a  $\beta$  matrix with  $\gamma'$  platelets and refractory-rich (W and Re) phases, while the layer beneath comprises  $\gamma'$  phase and blocky refractory-rich precipitates. Solutioning is carried out in the  $\gamma$ -phase field;

therefore, at 1633 K (1360 °C), the microstructure comprises  $\gamma$ -phase with intermittent un-dissolved  $\gamma/\gamma'$  eutectic channels that intersect the surface and in some cases a layer of eutectic proud of the secondary dendrite arms.<sup>[18]</sup> During solutioning (ramp-up and isothermal hold), there is a phase transformation that occurs within the outermost surface layer;  $\gamma \rightarrow \gamma' \rightarrow \beta$ . De-stabilization of  $\gamma$ -phase requires significant depletion of Ni where in the preceding section, it has been shown that this Ni loss occurs through vaporization. The Ni loss cannot be accurately assessed, since the Langmuir equation does not consider elemental interactions in case of non-ideal solutions and only deals with vaporization in vacuum. From Figure 8, it is clear that vapor pressure increases with temperature and beyond 1523 K (1250 °C),  $p_{\text{Ni}}$  for both elemental vaporization of Ni or volatilisation of NiO  $\sim [10^{-8} - 10^{-7}]$  atm. Therefore, vaporization will occur at temperatures approaching the final solutioning temperature. Importantly, however, Ni loss from the surface would lead to subsequent solute re-distribution within the surface layers, so if vaporization kinetics are known, this can be coupled to solute diffusion equations to determine the phase evolution sequence within the substrate. However, unlike in the case of oxidation—where oxidation kinetics can be coupled with solute diffusion to determine the evolution of phases<sup>[27]</sup>—coupling of elemental loss with diffusion in the substrate is formidable for two principal reasons; (i) the vaporization rate is not constant, when more than one element is involved and elemental interactions occur and (ii) limited existence of experimental diffusion data in the case of congruently melting  $\gamma'$  and  $\beta$ -phase.<sup>[28, 29]</sup> Therefore, to predict the phase evolution sequence, a simplified first-order approach will be adopted, where the processes of vaporization and resultant diffusion in the substrate will be considered independently.

The Ni-foil experiment is first considered. In this case, the distinct absence of the  $\beta$  condensate indicates that the principal vaporizing species is Ni and which simplifies the approach. Since the surface polycrystalline layer comprises  $\gamma'$  and refractory-rich (W and Re) precipitates, an averaging approach can be adopted as described. Defining a ratio

$$\frac{1}{\alpha} = \left[ \frac{\text{Depth beneath surface from where Ni vaporizes}}{\text{Depth of substrate where inter-diffusion occurs with surface layer}} \right],$$

where perfect mixing is assumed to occur between layers of thickness 1 (depth of layer from where Ni loss occurs) and  $\alpha$  (layer of substrate), resulting in a new composition in a layer of thickness  $[1 + \alpha]$ . By using such an averaging approach, the kinetics of diffusion between the two layers can be incorporated through the term “ $\alpha$ ”, which is the width of the substrate; as the extent of inter-diffusion increases,  $\alpha \gg 1$ . The phase evolution is then determined corresponding to the composition of the region with thickness  $[1 + \alpha]$ . This approach tacitly assumes that since the loss of Ni from the surface layers will result in an increased mole-fraction of all other elements, stabilization of  $\gamma'$  results in incorporation of Al and Ta within  $\gamma'$ , while excess Cr, W, and Re are incorporated within the refractory-rich precipitates, such that mass balance is maintained. For the substrate composition, the nominal composition is considered, since it is clear from the experiments that microstructural instability occurs across the surface and independent of the surface composition. The phase distribution was calculated with the TTNi8 database using the Thermo-Calc software.<sup>[30]</sup> A summary of the phase evolution is presented in Table II, where for  $\alpha \leq 2$ , extensive melting (>50 pct) is predicted at the solutioning temperature. On quenching, a Scheil-type freezing can be assumed (very limited back-diffusion in the solid; Scheil assumes absence of back-diffusion), where the phase fraction for remnant 10 pct liquid is calculated and shows the marked de-stabilization of  $\gamma$  phase. However, a melted and subsequently re-frozen microstructure should necessarily have resulted in cellular growth morphology, with the cells growing from the unmelted substrate to the surface. The observed morphology is not in consonance with this requirement; here, the growth occurs *from the surface into the substrate* and hence categorically precludes the occurrence of melting. An increasing extent of inter-diffusion with the substrate during isothermal hold,  $2 < \alpha \leq 4$ , shows a marked dissolution of  $\gamma$  phase at the solutioning temperature, but with clear absence of melting. In fact, the phase fraction at 1273 K (1000 °C) shows the presence of P-Phase (W and Re-rich) and >85 pct  $\gamma'$ , with <10 pct  $\gamma$ . In fact remnant  $\gamma$ -phase is observed in Figure 6(a),

**Table II. Summary of Phase Evolution Corresponding to Vaporization and Subsequent Inter-diffusion with the Substrate for Different Ratios,  $\alpha$**

1: $\alpha$	Mole Pct at 1633 K (1360°C)	Scheil Freezing Path for Liquid (Remnant 10 pct) or Phase Fraction at 1273 K (1000 °C)
1:1	$L = 94.5, P = 4.5, \sigma = 1$	$\beta = 24, \gamma' = 63.5, \sigma = 1$ [1505 K (1232°C)]
1:2	$L = 57.2, \gamma' = 31.6, \gamma = 7, P = 4$	$\gamma = 18.8, \gamma' = 69.8, \sigma = 1.4$ [1564 K (1291 °C)]
1:3	$\gamma' = 56, \gamma = 42, P = 2$	$\gamma' = 94, \gamma = 0, P = 6$
1:4	$\gamma' = 38, \gamma = 61, P = 1$	$\gamma' = 86, \gamma = 9, P = 5$

where  $\gamma$ -channels are present within  $\gamma'$ -grains, as highlighted. This microstructure is markedly different from that observed within the bulk, which shows a near-cuboidal  $\gamma/\gamma'$  morphology, with  $\gamma' \sim 70$  pct, which is the desired microstructure for high-temperature creep strength.

In the case of the open-boat sample, it is not straightforward to adopt the procedure as in the previous case owing to the following reasons;

- (a) Vaporization of both Ni and Al occurs, albeit most likely in sequence. The stabilization of  $\beta$  phase at the surface (intermediate layer) results from the transformation  $\gamma \rightarrow \gamma' \rightarrow \beta$ .
- (b) Initial Ni loss is accompanied by the  $\gamma \rightarrow \gamma'$  transformation, and the evolution of the microstructure can be treated adequately as in the previous instance.
- (c) However, subsequent Ni loss results in the  $\gamma' \rightarrow \beta$  transformation but a simplistic treatment for this case is not straightforward. Ni loss from  $\gamma'$  (enriched in Ta and Al) will result in stabilization of  $\beta$  (enriched in Al); however,  $\beta$  has no solubility for Ta, requiring Ta diffusion into the bulk and therefore requiring a kinetic model, which is lacking in this treatment.

There are two aspects that are worthy of mention. First, the formation of  $\beta$  phase because of Ni-depletion is not unexpected; in fact it is worth pointing out that a study has reported the stabilization of  $\beta$  phase owing to the formation of NiO as a precursor to internal oxidation of CMSX10 at temperatures below 1273 K (1000 °C),<sup>[19]</sup> although the extent of coverage is not as extensive as in our experiments. Second, the de-stabilization of  $\gamma$  phase at the surface resulting in a  $\gamma'$  and TCP phase mixture is also commonly encountered during the aluminisation of Ni aerofoils typically at 1373 K (1100 °C).<sup>[31,32]</sup> Importantly in this case, the precipitate morphology is typical needle-shaped; this is also not surprising since the nucleation and growth of these precipitates occur at grain boundaries, and further, growth is driven by solute diffusion along the grain boundary, which is characteristic of discontinuous precipitation.<sup>[33]</sup> In the present experiments, it is clear that the nucleation and growth are volume-diffusion controlled, as these morphologies are observed at the solutioning temperature, 1633 K (1360 °C), where volume-diffusion predominates.

While formation of  $\beta$  phase (intermediate layer) can be rationalised by Ni loss, there is also the distinct presence of the  $\beta$  condensate (top layer), which is observed on top of the test bar surface and it is clear that this condensate formed on the surface during quench. Once  $\beta$  phase has formed at the surface, subsequently vaporization of Al also occurs from  $\beta$  phase, owing to the increased activity of Al, as has been reported.<sup>[34]</sup> Vaporization of Al will result in subsequent de-stabilization of  $\beta$  phase leading to nucleation of  $\gamma'$ -phase, and this platelet or lamellar morphology is distinctly observed within the outer zone at the surface of the test bar. Also, inter-diffusion of Al between the outer surface layer and the substrate will occur and this in turn

would result in de-stabilization of  $\gamma$ -phase in the substrate, and the excess W and Re will be accommodated by refractory-rich precipitates. However, neither vaporization of Al nor inter-diffusion of Al has been taken into account in the present work. The reason for the latter arises from the lack of necessary diffusion data of multi-component  $\beta$  and  $\gamma'$  phases. The assessment of the vaporization of Al requires vapor pressure corresponding to  $\beta$  phase at elevated temperatures. Both of these aspects will be considered in a subsequent study.

Finally, a very important point is worth emphasising. The only oxide observed after solutioning is  $\text{Al}_2\text{O}_3$ . In all the calculations quantifying the thermodynamic driving force for vaporization (Figure 8), the presence of  $\text{Al}_2\text{O}_3$  covering the surface has been neglected. This can be rationalised as follows—Oxide growth kinetics as given by the parabolic rate constant,  $k_p$  is significantly retarded in  $\alpha\text{-Al}_2\text{O}_3$  compared with other oxides, such as NiO or CoO.<sup>[20,21]</sup> In fact, initially transitional  $\text{Al}_2\text{O}_3$  forms by outward cation ( $\text{Al}^{3+}$ ) diffusion and eventually  $\alpha\text{-Al}_2\text{O}_3$  forms by internal oxidation, which is anion ( $\text{O}^{2-}$ ) controlled. Therefore, as long as there is no “continuous” coverage of the surface by  $\text{Al}_2\text{O}_3$ , vaporization will occur. Both vaporization and oxide formation therefore occur competitively, with vaporization dominating. The curves calculated in Figure 8 therefore correspond to regions where a “protective” layer of  $\text{Al}_2\text{O}_3$  has not formed. As the extent of  $\text{Al}_2\text{O}_3$  coverage increases, the kinetics of vaporization decreases.

## V. CONCLUSIONS

1. The development of micro-structural instability at the surface during solution heat treatment of a typical third-generation Ni-base superalloy, CMSX10N has been studied.
2. Vaporization of Ni occurs from the surface during solutioning in an Ar atmosphere, and subsequent solute re-distribution leads to de-stabilization of  $\gamma$  phase.
3. With increasing extent of vaporization, a phase mixture of  $\beta$ ,  $\gamma'$ , and the refractory (W and Re-rich) precipitates occur within the surface layers.
4. Conditions at the surface have a marked effect on the vaporization kinetics and subsequent evolution of phases. The presence of a dense oxide such as  $\text{Al}_2\text{O}_3$  or the presence of sacrificial Ni-foils interspersed in the furnace significantly suppresses elemental vaporization from the sample surface.
5. Thermodynamic calculations have been carried out to quantitatively describe the phase evolution during solutioning and after quenching.

## ACKNOWLEDGEMENT

The authors would like to thank Mr. Peter Cranmer and Mr. Shixiang Zhao during the course of experimental work.

## REFERENCES

1. G.L. Erickson: *J. Met.*, 1995, vol. 47, pp. 36–39.
2. H.T. Pang, H.B. Dong, R. Beanland, H.J. Stone, C.M.F. Rae, P.A. Midgley, G. Brewster, and N. D'Souza: *Metall. Mater. Trans. A*, 2009, vol. 40A, pp. 1660–69.
3. N. D'Souza and H.B. Dong: *Scripta Mater.*, 2007, vol. 56, pp. 41–44.
4. S.-M. Seo, J.-H. Lee, Y.-S. Yoo, C.-Y. Jo, H. Miyahara, and K. Ogi: in *Superalloys 2008*, R.C. Reed, K.A. Green, P. Caron, T. Gabb, M.G. Fahrman, E.S. Huron, and S.A. Woodard, eds., TMS, Warrendale, PA, 2008, pp. 277–86.
5. N. Warnken, D. Ma, M. Mathes, and I. Steinbach: *Mater. Sci. Eng., A*, 2005, vols. 413–414, pp. 267–71.
6. C. Walter, B. Hallstedt, and N. Warnken: *Mater. Sci. Eng., A*, 2005, vol. 397, pp. 385–90.
7. G.E. Fuchs: *Mater. Sci. Eng., A*, 2001, vol. 300A, pp. 52–60.
8. N. Warnken, H. Larrson, and R.C. Reed: *Mater. Sci. Tech.*, 2009, vol. 25, pp. 179–85.
9. S.L. Semiatin, R.C. Kramb, R.R. Turner, F. Zhang, and M.M. Anthony: *Scripta Met.*, 2004, vol. 51, pp. 491–95.
10. M.S.A. Karunaratne, D.C. Cox, P. Carter, and R.C. Reed: in *Superalloys 2000*, T.M. Pollock, R.D. Kissinger, R.R. Bowman, K.A. Green, M. McLean, S. Olson, and J.J. Schirra, eds., TMS, Warrendale, PA, 2000, pp. 201–10.
11. N. D'Souza, S. Simmonds, G.D. West, and H.B. Dong: *Metall. Mater. Trans. A*, 2013, vol. 44A, pp. 4764–73.
12. C.B. Alcock, V.P. Itken, and M.K. Horrigan: *Can. Met. Q.*, 1984, vol. 23, pp. 309–13.
13. *Heat Resistant Materials*, J.R. Davis, ed., ASM International, Issue 1, pp. 290–308, 1997.
14. J.R. Griffin and S.W. Kennedy: *Vacuum Technology—Practical heat treating and Brazing*, Roger Fabian ed., ASM International, Issue 1, pp. 1–24, 1993.
15. A. Powell, J. Van Den Avyle, B. Damkroger, J. Szekely, and U. Pal: *Metall. Mater. Trans. B*, 1997, vol. 28B, pp. 1227–39.
16. I. Langmuir: *Phys. Z.*, 1913, vol. 14, pp. 1273–80.
17. G. Brewster, N. D'Souza, K. Ryder, S. Simmonds, and H.B. Dong: *Metall. Mater. Trans. A*, 2012, vol. 43A, pp. 1288–302.
18. G. Brewster, H.B. Dong, N.R. Green, and N. D'Souza: *Metall. Mater. Trans. B*, 2008, vol. 39B, pp. 87–93.
19. C.M. Younes, G.C. Allen, and J.A. Nicholson: *Corr. Eng. Sci. Tech.*, 2002, vol. 27, pp. 80–88.
20. I.M. Edmonds, H.E. Evans, and C.N. Jones: in *Superalloys 2008*, R.C. Reed, K.A. Green, P. Caron, T. Gabb, M.G. Fahrman, E.S. Huron, and S.A. Woodard, eds., TMS, Warrendale, PA, 2008, pp. 661–70.
21. H.J. Grabke: *Intermetallics*, 1999, vol. 7, pp. 1153–58.
22. Y. Zhang, J.A. Haynes, B.A. Pint, I.G. Wright, and W.Y. Lee: *Surf Coat. Tech.*, 2003, vols. 163–164, pp. 19–24.
23. F.D. Richardson and J.H.E. Jeffes: *J. Iron Steel Inst.*, 1948, vol. 160, pp. 261–70.
24. A. Akhtar, M.S. Hook, and R.C. Reed: *Metall. Mater. Trans. A*, 2005, vol. 36A, pp. 3001–17.
25. S. Chevalier, A. Galerie, O. Heintz, R. Chassagnon, and A. Crisci: *Mater. Sci. Forum*, 2008, vols. 595–598, pp. 915–22.
26. H.E. Evans: *Int. Mater. Rev.*, 1995, vol. 40, pp. 1–40.
27. T.J. Nidjam and W. Sloof: *Acta Mater.*, 2008, vol. 56, pp. 4972–83.
28. K. Fujiwara and Z. Horita: *Acta Mater.*, 2002, vol. 50, pp. 1571–79.
29. C.E. Campbell: *Acta Mater.*, 2008, vol. 56, pp. 4277–90.
30. J.-O. Andersson, T. Helander, L. Hoglund, P.F. Shi, and B. Sundman, *CALPHAD*, Vol. 26, 2002, pp. 273–312. (TTNI8 database: <http://www.thermocalc.com/>).
31. C.M.F. Rae, M.S. Hook, and R.C. Reed: *Mater. Sci. Eng. A*, 2005, vol. 396, pp. 231–39.
32. W.S. Walston, J.C. Schaeffer, and W.H. Murphy: in *Superalloys 1996*, R.D. Kissinger, D.J. Deye, D.L. Anton, A.D. Cetel, M.V. Nathal, and T.M. Pollock, eds., TMS, Warrendale, PA, 1996, pp. 9–18.
33. J.D. Nystrom, T.M. Pollock, W.H. Murphy, and A. Garg: *Metall. Mater. Trans. A*, 1997, vol. 28A, pp. 2443–52.
34. L. Bencze, D.D. Raj, D. Kath, W.A. Oates, L. Singheiser, and K. Hilpert: *Metall. Mater. Trans. B*, 2004, vol. 35B, pp. 867–76.